

Non-perturbative renormalization of overlap quark bilinears on 2+1-flavor domain wall fermion configurations

Zhaofeng Liu¹, Ying Chen¹, Shao-Jing Dong², Michael Glatzmaier²,
Ming Gong², Anyi Li³, Keh-Fei Liu², Yi-Bo Yang¹ and Jian-Bo Zhang⁴
(χ QCD Collaboration)

¹Institute of High Energy Physics and Theoretical Physics Center for Science Facilities, Chinese Academy of Sciences, Beijing 100049, China

²Department of Physics and Astronomy, University of Kentucky, Lexington, KY 40506

³Institute for Nuclear Theory, University of Washington, Seattle, WA 98195

⁴Department of Physics, Zhejiang University, Hangzhou 311027, China

Abstract

We present renormalization constants of overlap quark bilinear operators on 2+1-flavor domain wall fermion configurations. This setup is being used by the χ QCD collaboration in calculations of physical quantities such as strangeness in the nucleon and the strange and charm quark masses. The scale independent renormalization constant for the axial vector current is computed using Ward Identity. The renormalization constants for scalar, pseudoscalar and vector current are calculated in the RI-MOM scheme. Results in the $\overline{\text{MS}}$ scheme are also given. The step scaling function of quark masses in the RI-MOM scheme is computed as well. The analysis uses in total six different ensembles of three sea quarks each on two lattices with sizes $24^3 \times 64$ and $32^3 \times 64$ at spacings $a = (1.73 \text{ GeV})^{-1}$ and $(2.28 \text{ GeV})^{-1}$, respectively.

1 Introduction

The overlap valence quark on 2+1 flavor domain wall fermion (DWF) configurations has been used to calculate the strangeness and charmness in the nucleon [1] with high precision. Due to the high degree of chiral symmetry of these fermions, the calculation of the strangeness content is free of the problem of large mixing with the $\bar{u}u$ and $\bar{d}d$ matrix elements due to the additive renormalization of the quark mass that plagues the Wilson fermions. In addition to having small $\mathcal{O}(a^2)$ discretization errors [2, 3], the overlap fermion that we use for the valence quarks in the nucleon can also be used for the light and charm quarks with small $\mathcal{O}(m^2 a^2)$ error [4, 5]. This allows us to calculate the charmonium and charm-light mesons in addition to strangeness and charmness contents. The inversion of overlap fermions can be speeded up by using HYP smearing [6] and deflation with low eigenmodes [5]. The χ QCD collaboration is determining charm and strange quark masses [7] and other physical quantities with the setup of overlap valence on DWF sea. The renormalization constants of quark bilinear operators needed to match lattice results to those in the continuum $\overline{\text{MS}}$ scheme are presented in this paper.

Non-perturbative renormalization is important in current lattice calculations aiming at percent level accuracy. As we know, the convergence of lattice perturbative calculations is often not satisfying and lattice perturbation series rarely extend beyond the one-loop level.

We use the RI-MOM scheme [8] to calculate renormalization constants for flavor non-singlet scalar, pseudoscalar, vector and axial vector operators $\mathcal{O} = \bar{\psi}\Gamma\psi'$, where $\Gamma = I, \gamma_5, \gamma_\mu, \gamma_\mu\gamma_5$ respectively (we will use S, P, V, A to denote the four operators throughout this paper). The results are converted to the $\overline{\text{MS}}$ scheme using ratios from continuum perturbative calculations. Following Refs. [9, 10], we also calculate the step scaling function in the RI-MOM scheme for quark masses. In this way, the $\mathcal{O}(a^2)$ discretization errors are removed differently.

We have calculated the renormalization constants at two lattice spacings with $a^{-1} = 1.73(3)$ GeV and $2.28(3)$ GeV. At each lattice spacing, there are three light sea quark masses. At each light sea quark mass, we use eight valence quark masses. The final results are obtained in the chiral limit of both the sea and valence quark masses, which confirm $Z_S = Z_P$ and $Z_V = Z_A$ for overlap fermions. The main results of this work are given in Tabs. 3, 4, 5, 6, 7 and 8.

We consider the systematic errors carefully. A main source of systematic errors for Z_S comes from the truncation of the perturbative ratio from the RI-MOM scheme to the $\overline{\text{MS}}$ scheme. We obtain $Z_S^{\overline{\text{MS}}}(2 \text{ GeV}) = 1.127(9)(19)$ on the coarse lattice and $1.056(6)(24)$ on the fine lattice, where the first uncertainty is statistical and the second systematic.

This paper is organized as follows. In Sec. 2, we briefly review the RI-MOM scheme and the overlap formalism. The numerical results in the RI-MOM and $\overline{\text{MS}}$ schemes, the analysis of systematic errors and the calculation of the step scaling function are given in Sec. 3. Then we summarize and conclude with some general remarks in Sec. 4.

2 Methodology

The non-perturbative calculation of renormalization constants in the RI-MOM scheme [8] is based on imposing renormalization conditions on amputated Green functions of the relevant operators in the momentum space. The Green functions needed to be computed include the quark propagator

$$S(p) = \sum_x e^{-ipx} \langle \psi(x) \bar{\psi}(0) \rangle, \quad (1)$$

the forward Green function

$$G_{\mathcal{O}}(p) = \sum_{x,y} e^{-ip \cdot (x-y)} \langle \psi(x) \mathcal{O}(0) \bar{\psi}(y) \rangle, \quad (2)$$

and the vertex function

$$\Lambda_{\mathcal{O}}(p) = S^{-1}(p) G_{\mathcal{O}}(p) S^{-1}(p). \quad (3)$$

The renormalization condition requires that the renormalized vertex function at a given scale $p^2 = \mu^2$ coincides with its tree-level value. That is to say

$$Z_q^{-1} Z_{\mathcal{O}} \frac{1}{12} \text{Tr} [\Lambda_{\mathcal{O}}(p) \Lambda_{\mathcal{O}}^{tree}(p)^{-1}]_{p^2=\mu^2} = 1, \quad (4)$$

where Z_q is the quark field renormalization constant with $\psi_R = Z_q^{1/2} \psi$ (the subscript “R” means after renormalization) and $Z_{\mathcal{O}}$ the renormalization constant for operator \mathcal{O} with $\mathcal{O}_R = Z_{\mathcal{O}} \mathcal{O}$. Eq.(4) is defined in the quark massless limit so that RI-MOM is a mass independent renormalization scheme. In practice, we do calculations at finite quark masses and then extrapolate to the chiral limit. For convenience, a projected vertex function is defined by

$$\Gamma_{\mathcal{O}}(p) \equiv \frac{1}{12} \text{Tr} [\Lambda_{\mathcal{O}}(p) \Lambda_{\mathcal{O}}^{tree}(p)^{-1}]. \quad (5)$$

In the RI scheme, Z_q^{RI} can be determined by [8]

$$Z_q^{RI}(\mu) = \frac{-i}{48} \text{Tr} \left[\gamma_{\nu} \frac{\partial S^{-1}(p)}{\partial p_{\nu}} \right]_{p^2=\mu^2}. \quad (6)$$

This is consistent with Ward Identities so that the renormalization constant in the RI scheme for the conserved vector current is one. However on the lattice, it is not convenient to do derivatives with respect to the discretized momentum.

Following Ref. [11], we shall use the renormalization of the axial-vector current to set the scale. Since we can obtain the renormalization constant Z_A^{WI} of the local axial vector current from Ward Identities, which equals to Z_A^{RI} in the RI scheme, we can get Z_q^{RI} from

$$Z_q^{RI} = Z_A^{WI} \frac{1}{12} \text{Tr} [\Lambda_A(p) \Lambda_A^{tree}(p)^{-1}]_{p^2=\mu^2}. \quad (7)$$

Once we obtain Z_q^{RI} , we use Eq.(4) to get Z_S , Z_P and Z_V for the scalar, pseudoscalar and vector currents. At tree level, $\Lambda_{\mathcal{O}}^{tree}(p) = \Gamma$ for the quark bilinear operators.

The Green functions in Eq.(4) are not gauge invariant, therefore the calculation has to be done in a fixed gauge, usually in the Landau gauge.

The massless overlap operator [12] is defined as

$$D_{ov}(\rho) = 1 + \gamma_5 \varepsilon(\gamma_5 D_w(\rho)), \quad (8)$$

where ε is the matrix sign function and $D_w(\rho)$ is the usual Wilson fermion operator, except with a negative mass parameter $-\rho = 1/2\kappa - 4$ in which $\kappa_c < \kappa < 0.25$. We set $\kappa = 0.2$ in our calculation that corresponds to $\rho = 1.5$. The massive overlap Dirac operator is defined as

$$\begin{aligned} D_m &= \rho D_{ov}(\rho) + m \left(1 - \frac{D_{ov}(\rho)}{2}\right) \\ &= \rho + \frac{m}{2} + \left(\rho - \frac{m}{2}\right) \gamma_5 \varepsilon(\gamma_5 D_w(\rho)). \end{aligned} \quad (9)$$

To accommodate the $SU(3)$ chiral transformation, it is usually convenient to use the chirally regulated field $\hat{\psi} = (1 - \frac{1}{2}D_{ov})\psi$ in lieu of ψ in the interpolation field and the currents. This is equivalent to leaving the unmodified currents and instead adopting the effective propagator

$$G \equiv D_{eff}^{-1} \equiv \left(1 - \frac{D_{ov}}{2}\right) D_m^{-1} = \frac{1}{D_c + m}, \quad (10)$$

where $D_c = \frac{\rho D_{ov}}{1 - D_{ov}/2}$ is chiral, i.e. $\{\gamma_5, D_c\} = 0$ [13]. With the good chiral properties of overlap fermions, we should get $Z_S = Z_P$ and $Z_V = Z_A$. These relations are well satisfied within uncertainties by our numerical results as will be shown later.

3 Numerical results

Our configurations are generated by the RBC-UKQCD collaboration using 2+1 flavor domain wall fermions[14, 15]. The lattice sizes are $24^3 \times 64$ and $32^3 \times 64$. On each lattice, there are three different light sea quark masses. On the $24^3 \times 64$ lattice they are $m_l/m_s = 0.005/0.04, 0.01/0.04$ and $0.02/0.04$ in lattice units. On the $32^3 \times 64$ lattice, $m_l/m_s = 0.004/0.03, 0.006/0.03$ and $0.008/0.03$. We employ one HYP smearing on the gauge fields [5] and then fix to the Landau gauge. The corresponding rotation matrices are saved. Then the quark propagators in the Landau gauge are rotated from those already computed before the gauge fixing to save time by avoiding doing inversions. The effects of smearing (one or only a few iterations) on observables go away in the continuum limit. Also, note that HYP smearing and gauge rotation on a configuration commute. Thus the effects in vertex functions of doing smearing before or after gauge fixing, or not doing smearing at all differ by discretization effects at a fixed lattice spacing. In Tab. 1, we give the number of configurations used in this work on each data ensemble. The overlap valence

Table 1: The number of configurations used in this work on the $24^3 \times 64$ and $32^3 \times 64$ lattices. The residual masses of DWF in lattice units m_{res} are in the two-flavor chiral limit as given in Ref. [14].

label	m_l/m_s	volume	N_{conf}	m_{res}
c005	0.005/0.04	$24^3 \times 64$	92	0.003152(43)
c01	0.01/0.04	$24^3 \times 64$	88	
c02	0.02/0.04	$24^3 \times 64$	138	
f004	0.004/0.03	$32^3 \times 64$	50	0.0006664(76)
f006	0.006/0.03	$32^3 \times 64$	40	
f008	0.008/0.03	$32^3 \times 64$	50	

Table 2: Overlap valence quark masses in lattice units on the $24^3 \times 64$ and $32^3 \times 64$ lattices.

$24^3 \times 64$	0.00620	0.00809	0.01020	0.01350	0.01720	0.02430	0.03650	0.04890
$32^3 \times 64$	0.00460	0.00585	0.00677	0.00885	0.01290	0.01800	0.02400	0.03600

quark masses in lattice units are given in Tab. 2. The corresponding pion masses are from about 220 to 600 MeV.

We use anti-periodic boundary condition in the time direction and periodic boundary condition in the spacial directions. Therefore the momenta are

$$ap = \left(\frac{2\pi k_1}{L}, \frac{2\pi k_2}{L}, \frac{2\pi k_3}{L}, \frac{(2k_4 + 1)\pi}{T} \right), \quad (11)$$

where $k_\mu = -6, -5, \dots, 6$ on the $L = 24$ lattice and $k_i = -6, -7, \dots, 6$, $k_4 = -5, -1, \dots, 6$ on the $L = 32$ lattice. To reduce the effects of Lorentz non-invariant discretization errors, we only use the momenta which satisfy the condition

$$\frac{p^{[4]}}{(p^2)^2} < 0.32, \quad \text{where } p^{[n]} = \sum_{\mu=1}^4 p_\mu^n, \quad p^2 = \sum_{\mu} p_\mu^2. \quad (12)$$

In other words, only those momenta pointing close to the diagonal direction are used. However as the statistical error decreases (for example, by using momentum sources [19]), the effects proportional to $a^2 p^{[4]}/p^2$ can be seen. To use all momenta and systematically remove the hypercubic effects, one can follow the method used in Refs. [16, 17]. Another way is to follow Ref. [9]. One can also use perturbative calculations to subtract and suppress those effects as, for example, in Ref. [18].

In our calculation, we require same p_4 , $p^{[4]}$ and $p^{[6]}$ when averaging momentum modes with a same p^2 . Therefore we can estimate the $\mathcal{O}(a^2 p^{[4]}/p^2)$ lattice artifacts (ignoring higher terms).

As we will show later, those effects are not small in Z_S . But because the condition in Eq.(12) is used, the $\mathcal{O}(a^2 p^{[4]}/p^2)$ effects can be absorbed into a simple $\mathcal{O}(a^2 p^2)$ term within our statistical uncertainty.

We use point source propagators in the Landau gauge to evaluate all the necessary Green functions and vertex functions. Momentum sources [19] can be used to improve the signal-to-noise ratio. But for each momentum one inversion is needed, which is expensive for overlap fermions. Thus we use the point source propagators which can be projected to many momenta. The statistical errors of our final results are from Jackknife processes.

3.1 Renormalization of the axial vector current from Ward identity

The renormalization constant Z_A can be obtained from the axial Ward identity

$$Z_A \partial_\mu A_\mu = 2Z_m m_q Z_P P, \quad (13)$$

where A_μ and P are the local axial vector current and the pseudoscalar density and Z_m is the quark mass renormalization constant with the renormalized mass $m_R = Z_m m_q$. Since $Z_m = Z_P^{-1}$ for overlap fermions, one can find Z_A by considering the matrix elements of the both sides of Eq.(13) between the vacuum and a pion

$$Z_A \partial_\mu \langle 0 | A_\mu | \pi \rangle = 2m_q \langle 0 | P | \pi \rangle. \quad (14)$$

If the pion is at rest, then from the above equation one gets

$$Z_A = \frac{2m_q \langle 0 | P | \pi \rangle}{m_\pi \langle 0 | A_4 | \pi \rangle}, \quad (15)$$

where $A_4 = \bar{\psi} \gamma_4 \gamma_5 \hat{\psi}$ and $P = \bar{\psi} \gamma_5 \hat{\psi}$. To obtain the matrix elements, we compute 2-point correlators

$$G_{PP}(\vec{p} = 0, t) = \sum_{\vec{x}} \langle 0 | P(x) P^\dagger(0) | 0 \rangle, \quad (16)$$

and

$$G_{A_4 P}(\vec{p} = 0, t) = \sum_{\vec{x}} \langle 0 | A_4(x) P^\dagger(0) | 0 \rangle. \quad (17)$$

When the time t is large, the contribution from the pion dominates in both correlators. Then one has

$$Z_A^{WI} = \lim_{m_q \rightarrow 0, t \rightarrow \infty} \frac{2m_q G_{PP}(\vec{p} = 0, t)}{m_\pi G_{A_4 P}(\vec{p} = 0, t)}. \quad (18)$$

In Fig. 1 we show examples of Z_A^{WI} obtained from Eq.(18) before taking the valence quark massless limit (denoted as $Z_A^{WI}(am_q)$). To take the limit $m_q \rightarrow 0$, we fit the data to [11]

$$Z_A^{WI}(am_q) = Z_A^{WI}(1 + b_A am_q). \quad (19)$$

After taking the valence quark massless limit, we get the results of Z_A^{WI} as given in Tab. 3. In the last column of Tab. 3, the results at the light sea quark massless limit are obtained by a linear extrapolation in $m_l + m_{res}$, where m_{res} is given in Tab. 1.

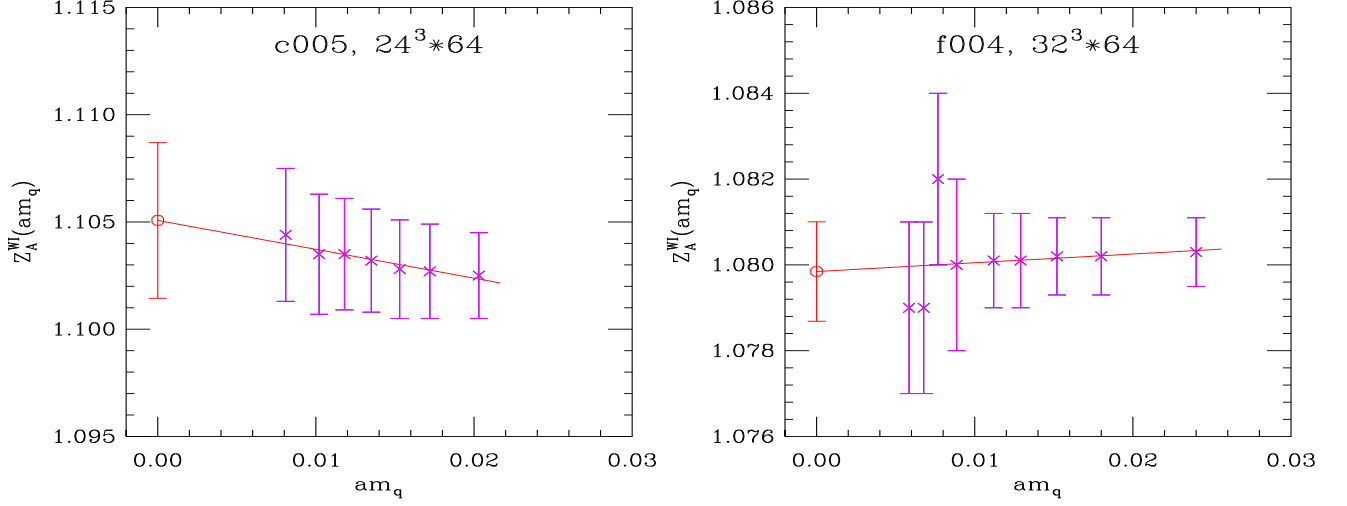


Figure 1: Examples of $Z_A^{WI}(am_q)$ against valence quark masses. The left graph is for the $L = 24$ lattice with sea quark masses $m_l/m_s = 0.005/0.04$. The right one for the $L = 32$ lattice with $m_l/m_s = 0.004/0.03$.

Table 3: Z_A^{WI} on the $24^3 \times 64$ and $32^3 \times 64$ lattices.

$24^3 \times 64$	m_l/m_s	0.02/0.04	0.01/0.04	0.005/0.04	$m_l + m_{res} = 0$
	Z_A^{WI}	1.101(4)	1.115(6)	1.105(4)	1.111(6)
$32^3 \times 64$	m_l/m_s	0.008/0.03	0.006/0.03	0.004/0.03	$m_l + m_{res} = 0$
	Z_A^{WI}	1.075(1)	1.079(1)	1.080(1)	1.086(2)

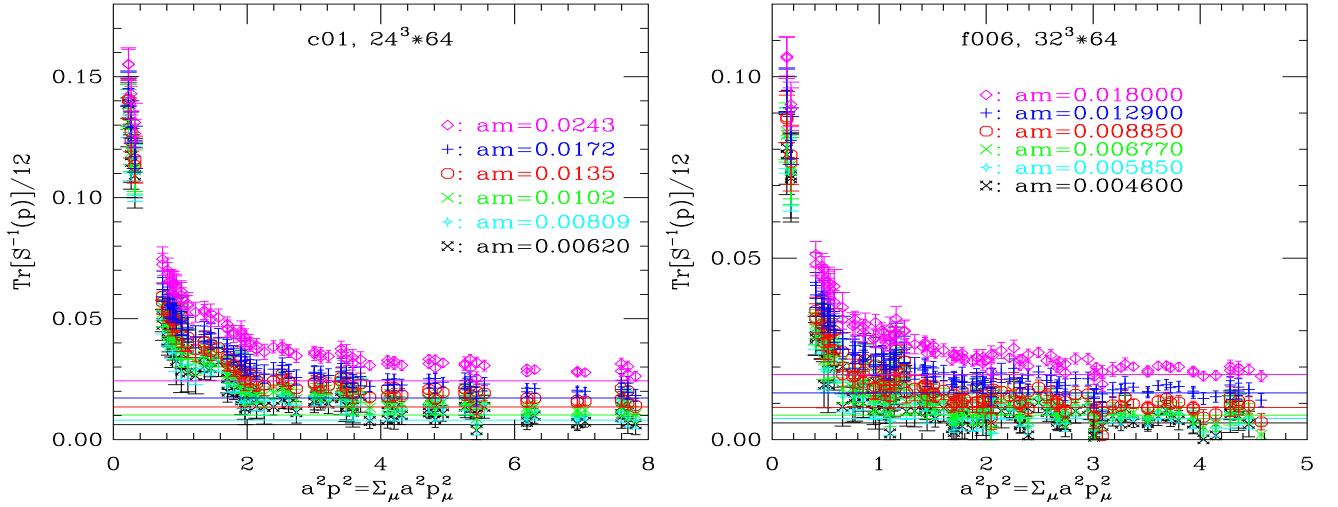


Figure 2: Examples of $\text{Tr}(S^{-1}(p))/12$ as functions of the momentum scale for different bare valence quark masses. The left graph is for the $L = 24$ lattice with sea quark masses $m_l/m_s = 0.01/0.04$. The right one for the $L = 32$ lattice with $m_l/m_s = 0.006/0.03$. The horizontal lines are the positions of the bare quark masses.

3.2 Analysis of the quark propagator

At large momentum, because of asymptotic freedom the quark propagator $S(p)$ goes back to the free quark propagator. In Fig. 2 we show examples of $\text{Tr}(S^{-1}(p))/12$ as functions of the momentum scale for different bare valence quark masses. As expected, $\text{Tr}(S^{-1}(p))/12$ goes to the bare quark mass value as the momentum scale increases. The two graphs in Fig. 2 are for data ensemble c01 and f006 respectively. The results from other ensembles are similar.

Fig. 3 shows examples of the quark field renormalization constants Z_q^{RI} as functions of the momentum scale for different valence quark masses. Z_q^{RI} is computed from Eq.(7). As we can see, the quark mass dependence of Z_q^{RI} is quite small on both the $L = 24$ and 32 lattices. The symbols in Fig. 3 are on top of each other except at very small $a^2 p^2$.

In Landau gauge, the anomalous dimension of Z_q is zero at 1-loop. This is why in Fig. 3 the behavior of Z_q is quite flat up to $\mathcal{O}(a^2 p^2)$ discretization errors.

3.3 Scalar density

After obtaining Z_q^{RI} , one can now get Z_S^{RI} from Eq.(4). The projected vertex function Γ_S (defined in Eq.(5)) and Z_S^{RI} as functions of the momentum scale for different valence quark masses on ensemble f006 are shown in Fig. 4.

Fig. 5 shows Z_S^{RI} as a function of the valence quark mass at different momentum for ensemble c01. Apparently, the dependence on am_q is not linear. Thus to go to the chiral limit, we use

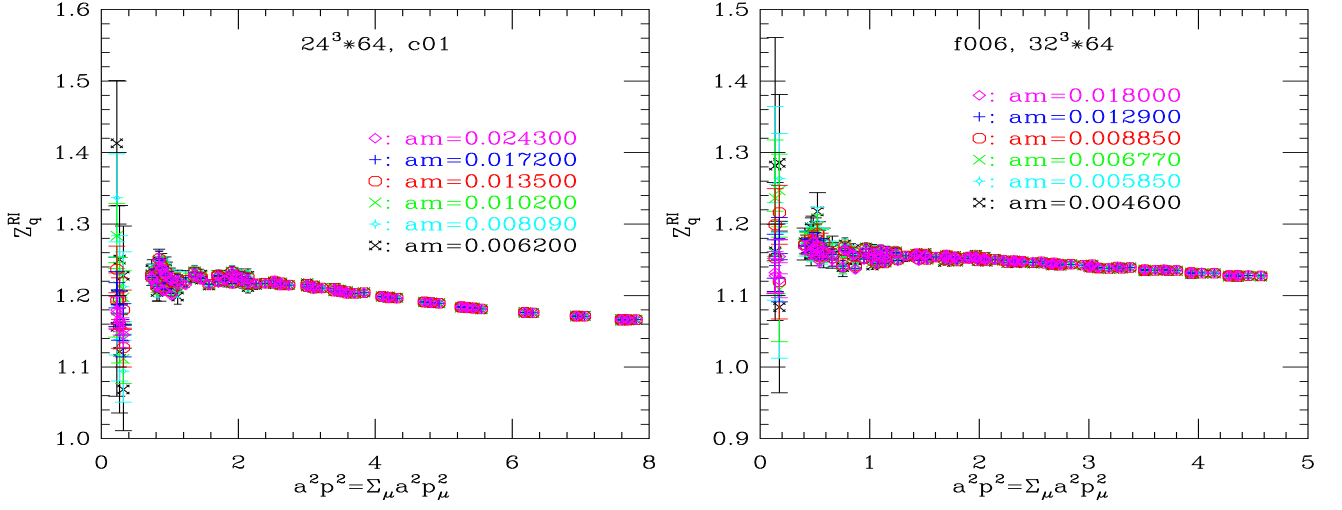


Figure 3: Examples of Z_q^{RI} as functions of the momentum scale for different valence quark masses. The left graph is for the $L = 24$ lattice with sea quark masses $m_l/m_s = 0.01/0.04$. The right one for the $L = 32$ lattice with $m_l/m_s = 0.006/0.03$.

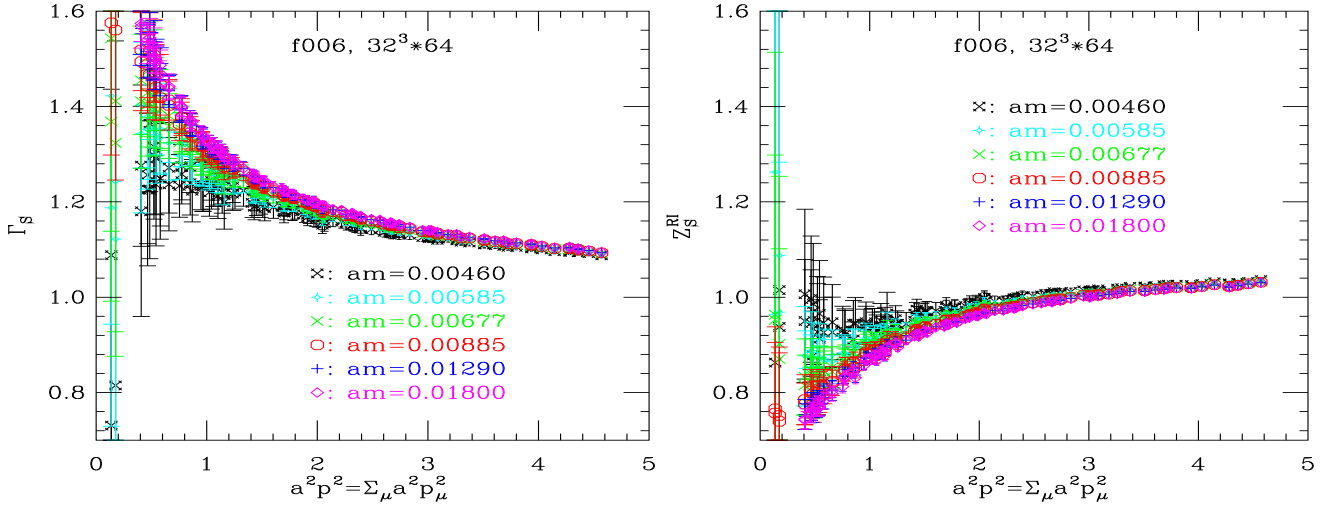


Figure 4: Examples of the projected vertex function Γ_S and Z_S^{RI} as functions of the momentum scale for ensemble f006.

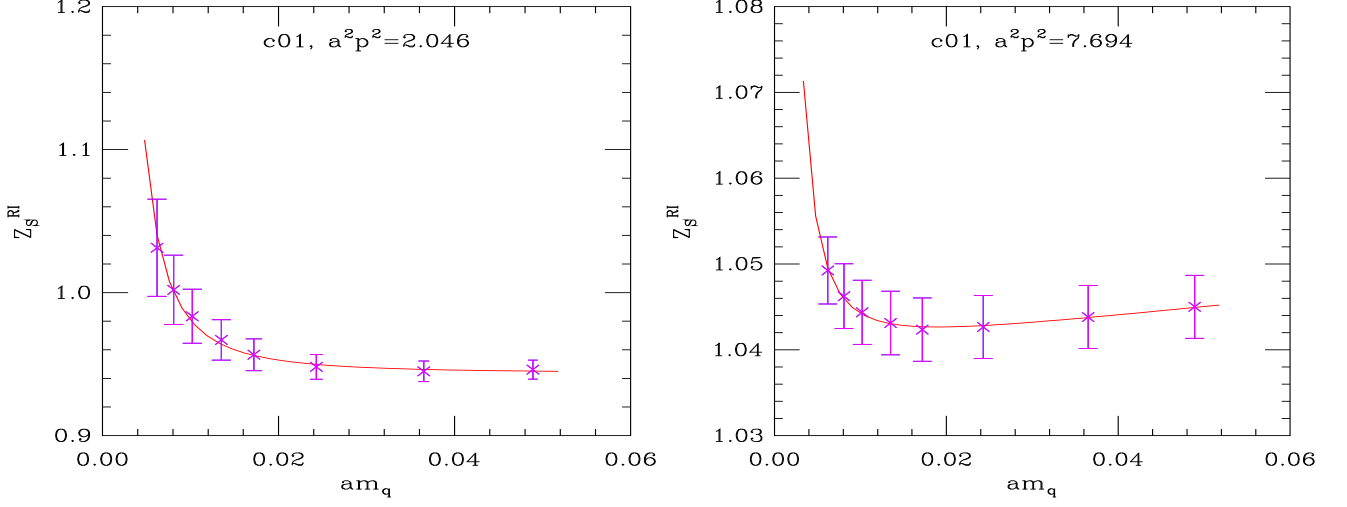


Figure 5: Z_S^{RI} as a function of the valence quark mass at two momentum scales for ensemble c01. The curves are fits to Eq.(20).

$$Z_S = \frac{A_s}{(am_q)^2} + B_s + C_s(am_q) \quad (20)$$

to fit our data and take B_s as the chiral limit value of Z_S . This fit function is inspired from Refs. [20, 21]. The double pole term in the above equation comes from the topological zero modes of the overlap fermions. In a calculation of Z_S in the RI' scheme [22], the curving up of Z_S at small valence quark mass is suppressed when the zero modes are subtracted from the quark propagator.

The fits of the data to Eq.(20) have small χ^2/dof at all momentum scales. Examples are shown in Fig. 5. The results of Z_S^{RI} in the valence quark massless limit as a function of the momentum scale for ensemble c005 are shown by the black diamonds in the left panel of Fig. 6.

Then one can use conversion ratios calculated in continuum perturbation theory to convert Z_S^{RI} into the $\overline{\text{MS}}$ scheme. In the quark massless limit, in Landau gauge and to three loops, the conversion ratio for Z_S and Z_P is [23, 24]

$$\begin{aligned} \frac{Z_S^{RI}}{Z_S^{\overline{\text{MS}}}} &= \frac{Z_P^{RI}}{Z_P^{\overline{\text{MS}}}} = 1 - \frac{16}{3} \frac{\alpha_s}{4\pi} + \left(-\frac{1990}{9} + \frac{89n_f}{9} + \frac{152\zeta_3}{3} \right) \left(\frac{\alpha_s}{4\pi} \right)^2 \\ &+ \left(-\frac{6663911}{648} + \frac{236650n_f}{243} - \frac{8918n_f^2}{729} + \frac{408007\zeta_3}{108} \right. \\ &\left. - \frac{4936\zeta_3 n_f}{27} - \frac{32\zeta_3 n_f^2}{27} + \frac{80\zeta_4 n_f}{3} - \frac{2960\zeta_5}{9} \right) \left(\frac{\alpha_s}{4\pi} \right)^3 + O(\alpha_s^4), \end{aligned} \quad (21)$$

where n_f is the number of flavors and ζ_n is the Riemann zeta function evaluated at n .

The value of $\alpha_s(\mu)$ is obtained by using its perturbative running to four loops [25]. The β -function in the $\overline{\text{MS}}$ scheme to 4-loops is given in Ref. [26]. We take the value $\Lambda_{QCD}^{\overline{\text{MS}}} = 339(10)$

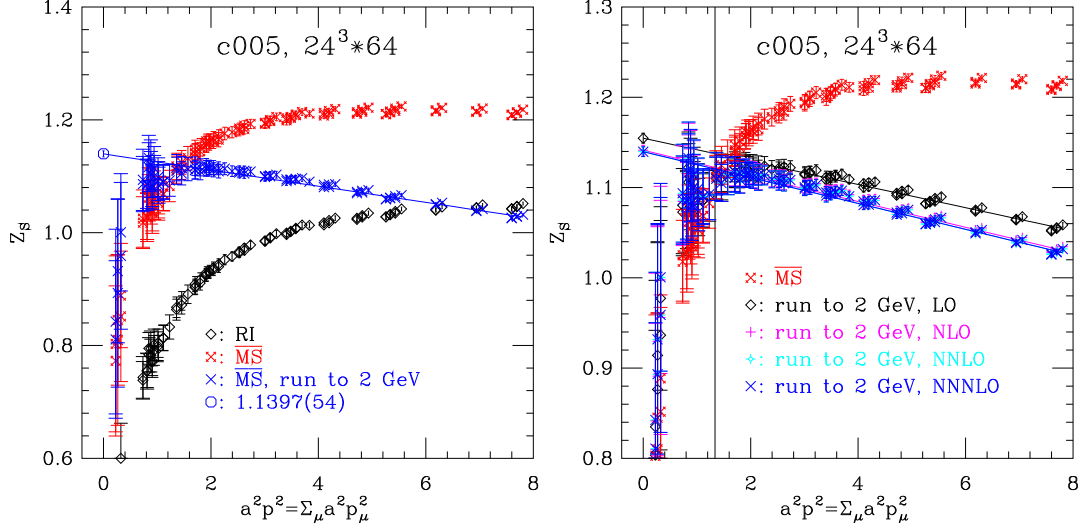


Figure 6: The conversion and running of Z_S in the valence quark massless limit on ensemble c005. Left panel: The black diamonds are the values in the RI scheme. The red fancy crosses are those in the $\overline{\text{MS}}$ scheme. The blue crosses are the results evolved to 2 GeV in the $\overline{\text{MS}}$ scheme as a function of the initial renormalization scale. Right panel: Comparison of the different orders of perturbative running in the $\overline{\text{MS}}$ scheme. The vertical line indicates $p = 2$ GeV.

MeV for three flavors in the $\overline{\text{MS}}$ scheme [27] to evaluate Eq.(21) numerically. For example, the strong coupling constant at 2 GeV is $\alpha_s^{\overline{\text{MS}}}(2 \text{ GeV}) = 0.2787$. The $\overline{\text{MS}}$ value $Z_S^{\overline{\text{MS}}}$ as a function of the scale $a^2 p^2$ are shown by the red fancy crosses in the left graph of Fig. 6.

To obtain $Z_S^{\overline{\text{MS}}}(2 \text{ GeV})$, we first use the anomalous dimension to four loops to evolve $Z_S^{\overline{\text{MS}}}(a^2 p^2)$ at the initial renormalization scale ap to 2 GeV (inverse lattice spacings $1/a = 1.73 \text{ GeV}$ and 2.28 GeV are used respectively). Since $Z_S = Z_m^{-1}$, we can use the mass anomalous dimension given in Ref. [24] for the perturbative running. The blue crosses in the left graph of Fig. 6 show $Z_S^{\overline{\text{MS}}}(2 \text{ GeV}; a^2 p^2)$, which are the 4-loop running results from the initial renormalization scale ap to the scale 2 GeV. $Z_S^{\overline{\text{MS}}}(2 \text{ GeV}; a^2 p^2)$ would lie on a horizontal line at large $a^2 p^2$ if there were no discretization errors (and if the truncation error of the conversion ratio is small).

The solid blue line in the left panel of Fig. 6 is a linear fit to the blue crosses with $a^2 p^2 > 5$. This is to reduce $\mathcal{O}(a^2 p^2)$ discretization errors. After the extrapolation we obtain $Z_S^{\overline{\text{MS}}}(2 \text{ GeV}) = 1.1397(54)$ for c005, where the error is only statistical. If we use the blue crosses with $a^2 p^2 > 4$ to do the extrapolation, then we find $Z_S^{\overline{\text{MS}}}(2 \text{ GeV}) = 1.1451(34)$. The two numbers are in agreement at one sigma. The difference introduced by the different range of $a^2 p^2$ will be included in the systematic errors of our final results.

In the right panel of Fig. 6, we compare the different orders of perturbative running in the $\overline{\text{MS}}$ scheme. As we can see, the truncation error is quite small after 2-loops. Only the 1-loop

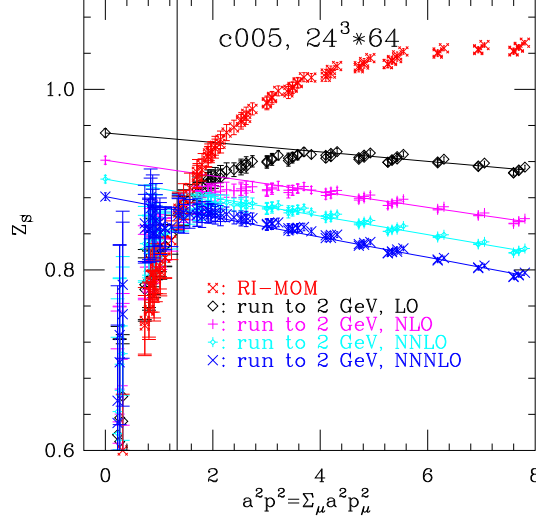


Figure 7: Comparison of the different orders of perturbative running in the RI-MOM scheme. The vertical line indicates $p = 2$ GeV.

running results do not agree with the 4-loop (NNNLO) running results. This is in contrast with the truncation error of running in the RI-MOM scheme, which we show in Fig. 7. The perturbative truncation error for the running of Z_S^{RI} is large even with 4-loops: The 3-loop and 4-loop results are different from each other. Similar behavior was also shown in Ref. [28]. With the much better running behavior in the $\overline{\text{MS}}$ scheme, it is preferred not to do the perturbative running of Z_S in the RI-MOM scheme. Nevertheless, if we use the $a^2 p^2$ extrapolated result $Z_S^{\text{RI}}(2 \text{ GeV}) = 0.8812(41)$ after the 4-loop running and the conversion ratio 1.289614 from Eq.(21) at 2 GeV from the RI to the $\overline{\text{MS}}$ scheme, we obtain $Z_S^{\overline{\text{MS}}}(2 \text{ GeV}) = 1.1364(53)$. This is in agreement with the above 1.1397(54).

We do a self-consistency check in Fig. 8 for the $a^2 p^2$ extrapolation after the running in the $\overline{\text{MS}}$ scheme. The black diamonds in the graph are $Z_S^{\overline{\text{MS}}}(p)$ at $p = 2, 2.5, 3, 3.5, 4, 4.5, 5$ GeV obtained from $a^2 p^2$ extrapolations after the running in the $\overline{\text{MS}}$ scheme as described above for getting $Z_S^{\overline{\text{MS}}}(p = 2 \text{ GeV})$. If the extrapolation works in reducing discretization errors, then the black diamonds should be well described by perturbative running in the $\overline{\text{MS}}$ scheme. We run down the black diamonds to 2 GeV using the 4-loop perturbative running in the $\overline{\text{MS}}$ scheme. The results are the magenta pluses which lie on a horizontal line within errors. This indicates that the $a^2 p^2$ extrapolation can indeed reduce $\mathcal{O}(a^2 p^2)$ discretization effects and the higher order effects are small.

The blue crosses in Fig. 6(left panel) do not necessary have a same $p^{[4]}/(p^2)^2$ value because the momentum modes we use are not exactly in a same direction. To see how the difference in

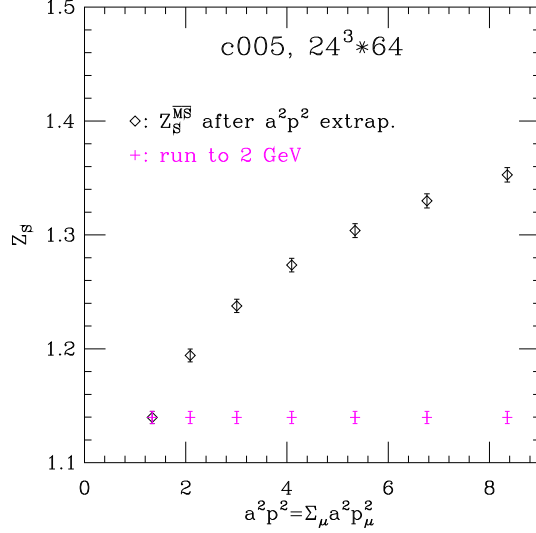


Figure 8: Self-consistency check for the $a^2 p^2$ extrapolation in the $\overline{\text{MS}}$ scheme. See text.

$p^{[4]}/(p^2)^2$ affects our final result, we use the three term function

$$\mathcal{Z}_S = Z_S + c_1(a^2 p^2) + c_2 \frac{a^2 p^{[4]}}{p^2} \quad (22)$$

to fit the blue crosses in Fig. 6(left panel) with $a^2 p^2 > 5$. Here other possible terms proportional to $a^2 p^{[6]}/(p^2)^2$, $a^4(p^2)^2$, etc. are ignored since Eq.(22) can already fit the data. The comparison of the three term fit with the $a^2 p^2$ extrapolation is shown in Fig. 9. Compared with the simple $a^2 p^2$ extrapolation, the three term fit decreases χ^2/dof visibly. The red line in Fig. 9 shows the fit function with the third term $c_2 \frac{a^2 p^{[4]}}{p^2}$ subtracted. The $\mathcal{O}(a^2 p^{[4]}/p^2)$ effects are not small since the red line is quite different from the blue data points. However from the three term fit we get $Z_S^{\overline{\text{MS}}}(2 \text{ GeV}) = 1.1372(54)$, which is in good agreement with $1.1397(54)$ from the $a^2 p^2$ extrapolation. This means with our statistical errors and with the condition in Eq.(12), the effects due to the difference in the directions of the momenta can be ignored.

Comparing the slope in our $a^2 p^2$ extrapolation with that in figure 2 of Aoki [28] (with NNNLO perturbative running), we find a larger a^2 effect in our data. Similar size of slopes were also seen in Refs. [29, 30], where gauge fields were also smeared, for renormalization constants. It is possible that our gauge smearing is related to the size of the slope in the $a^2 p^2$ extrapolation. It is discussed in Ref. [10] that link smearing may lower the upper end of the RI-MOM window and enhance a^2 effects. A study to compare our results with thin link results would be interesting to understand better the slope.

The values of $Z_S^{\overline{\text{MS}}}(2 \text{ GeV})$ on all ensembles are collected in Tab. 4, where we have used $a^2 p^2 > 5$ for the $a^2 p^2$ extrapolations on the $L = 24$ lattices and $a^2 p^2 > 3$ on the $L = 32$ lattices.

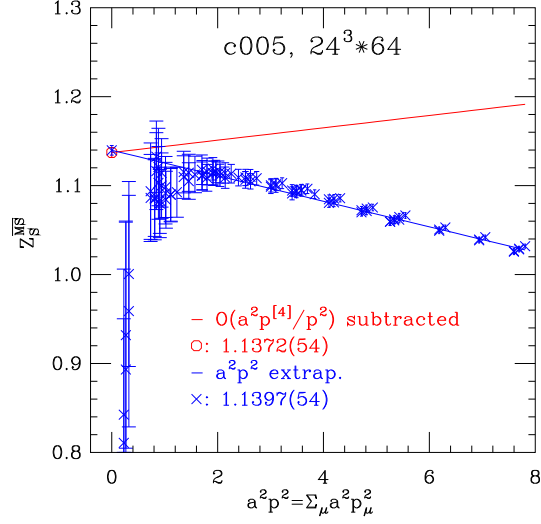


Figure 9: Comparison of the three term fit Eq.(22) with the $a^2 p^2$ extrapolation. The blue crosses are the results evolved to 2 GeV in the $\overline{\text{MS}}$ scheme as a function of the initial renormalization scale. The red line shows the three term fit function with the third term $c_2 \frac{a^2 p^{[4]}}{p^2}$ subtracted. The blue line is the $a^2 p^2$ extrapolation.

Table 4: $Z_S^{\overline{\text{MS}}}(2 \text{ GeV})$ on the $24^3 \times 64$ and $32^3 \times 64$ lattices.

ensemble	c02	c01	c005	$m_l + m_{res} = 0$
$Z_S^{\overline{\text{MS}}}(2 \text{ GeV})$	1.1545(74)	1.1361(82)	1.1397(54)	1.1272(87)
ensemble	f008	f006	f004	$m_l + m_{res} = 0$
$Z_S^{\overline{\text{MS}}}(2 \text{ GeV})$	1.074(10)	1.0714(64)	1.0574(65)	1.0563(64)

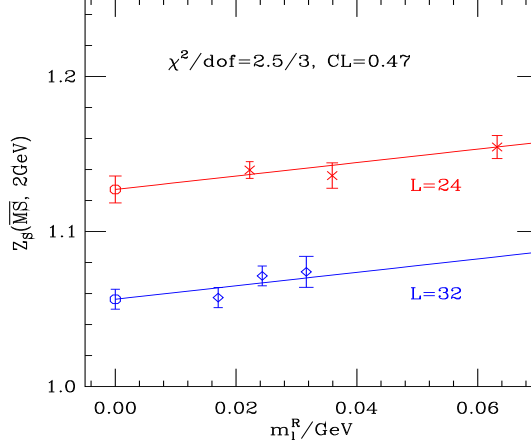


Figure 10: Linear extrapolation of $Z_S^{\overline{\text{MS}}}$ to the light sea quark massless limit.

From the values on all six ensembles with different sea quark masses on the $L = 24$ and 32 lattices, we do a simultaneous linear extrapolation in the renormalized light sea quark mass to obtain $Z_S^{\overline{\text{MS}}}$ in the sea quark massless limit. The fit function is

$$Z(m_l^R) = Z(0) + c \cdot m_l^R, \quad \text{where } m_l^R = (m_l + m_{res})Z_m^{sea}. \quad (23)$$

Here $Z_m^{sea} = 1.578(2)$ on the $L = 24$ lattice and $1.573(2)$ on the $L = 32$ lattice were given in Ref. [14]. The slopes of the two lines for the coarse and fine lattices are required to be the same.

The extrapolation is shown in Fig. 10, which has a good χ^2/dof . We do the simultaneous fit because the three light sea quark masses on the $L = 32$ lattice are close to each other and thus the data have less control on the slope. Finally we get $Z_S^{\overline{\text{MS}}}(L = 24) = 1.1272(87)$ and $Z_m^{\overline{\text{MS}}}(L = 24) = 1/Z_S^{\overline{\text{MS}}} = 0.887(7)$ at 2 GeV. For the fine lattice we find $Z_S^{\overline{\text{MS}}}(L = 32) = 1.0563(64)$ and $Z_m^{\overline{\text{MS}}}(L = 32) = 0.947(6)$.

We also did separate linear extrapolations in light sea quark masses on the coarse and fine lattices. The results are in agreement with those from the simultaneous fit. The change in the center values will be taken as one source of the systematic errors as discussed below.

Besides the statistical error, we consider the following systematic errors of Z_S . The error budget of Z_S in the chiral limit is given in Tab. 5.

First of all, high order terms that were ignored in the conversion ratio, Eq.(21), from the RI scheme to the $\overline{\text{MS}}$ scheme give truncation errors. To reduce this error, one uses Z_S^{RI} at large $a^2 p^2$. In our work, we use $a^2 p^2 > 5$ on the $L = 24$ lattice which means $p > 3.87$ GeV. On the $L = 32$ lattice, we use $a^2 p^2 > 3$ or $p > 4.02$ GeV. At $p = 4$ GeV, the numerical value of Eq.(21) is

$$\begin{aligned} \frac{Z_S^{\text{RI}}}{Z_S^{\overline{\text{MS}}}}(p = 4 \text{ GeV}, n_f = 3) &= 1 - 0.424\alpha_s - 0.827\alpha_s^2 - 1.944\alpha_s^3 + \dots \\ &= 1 - 0.092 - 0.039 - 0.020 + \dots, \end{aligned} \quad (24)$$

Table 5: Error budget of $Z_S^{\overline{\text{MS}}}(2 \text{ GeV})$ in the chiral limit

Source	Error (% , L=24)	Error (% , L=32)
Statistical	0.8	0.6
Truncation (RI to $\overline{\text{MS}}$)	1.5	1.4
Coupling constant	0.3	0.3
Perturbative running	<0.02	<0.02
Lattice spacing	0.5	0.4
Fit range of $a^2 p^2$	0.4	0.1
Extrapolation in m_l^R	0.2	1.8
Total systematic uncertainty	1.7	2.3

where we have used $\alpha_s^{\overline{\text{MS}}}(4 \text{ GeV}) = 0.2160$. The $\mathcal{O}(\alpha_s^3)$ term is about 2.4% of the total ratio. The ignored $\mathcal{O}(\alpha_s^4)$ term is further suppressed by a factor of α_s . Assuming its coefficient is 3 times large as that for the $\mathcal{O}(\alpha_s^3)$ term, we get a $\sim 1.5\%$ truncation error.

The uncertainty of the coupling constant α_s in Eq.(21) is another source of error. If we use $\Lambda_{\overline{QCD}}^{\overline{\text{MS}}} = 349 \text{ MeV}$ instead of 339 MeV to evaluate α_s , the center value of $Z_S^{\overline{\text{MS}}}(2 \text{ GeV})$ changes by 0.3% on both lattices.

The perturbative running of $Z_S^{\overline{\text{MS}}}$ from an initial scale p to 2 GeV uses 4-loop results of the anomalous dimension. The $\mathcal{O}(\alpha_s^4)$ term contributes less than 0.02% to the total running in our range of the initial scale $a^2 p^2$. Thus this systematic error can be safely ignored.

To determine where 2 GeV is, we need the values of our lattice spacings. The variation of lattice spacings in the range of one sigma leads to $\sim 0.5\%$ change in $Z_S^{\overline{\text{MS}}}(2 \text{ GeV})$.

In the extrapolation of $Z_S^{\overline{\text{MS}}}(2 \text{ GeV}; a^2 p^2)$ to reduce $\mathcal{O}(a^2 p^2)$ discretization errors, the fit range of $a^2 p^2$ introduces 0.4% error on the $L = 24$ lattice and 0.1% error on the $L = 32$ lattice. Here we vary $a^2 p^2 > 5$ to > 4 on the $L = 24$ lattice and $a^2 p^2 > 3$ to > 2 on the $L = 32$ lattice.

Finally, we consider the error due to the extrapolation in the light sea quark mass. As mentioned above, one can do separate and simultaneous fits to the data on the coarse and fine lattices. The difference in the center values is taken as a systematic error.

In total, adding all systematic errors quadratically we find 1.7% error for Z_S on the coarse lattice and 2.3% on the fine lattice. Putting the statistical and systematic errors together, we have $Z_S^{\overline{\text{MS}}}(2 \text{ GeV}) = 1.127(9)(19)$ on the coarse lattice and $1.056(6)(24)$ on the fine lattice. The statistical error is much smaller than the systematic error.

3.4 Step scaling function of the quark mass

We can use the above obtained $Z_S^{\overline{\text{MS}}}(2 \text{ GeV})$ to determine strange and charm quark masses [7] in the $\overline{\text{MS}}$ scheme. Another way is to first consider the continuum limit of renormalized RI data (quark mass, for example) at a fixed physical scale and then convert to the $\overline{\text{MS}}$ scheme by perturbation

theory at a high enough scale. This strategy was used in, for example, Ref. [31]. In this way, a^2p^2 extrapolation of the renormalization constants at large p is not used to avoid possible lattice artifacts: the upper edge of the RI-MOM window may be reduced by link smearing [10].

To use the above strategy to determine quark masses, we need the RI-MOM step scaling function in the continuum limit to run up to a high scale where perturbative conversion ratio to the $\overline{\text{MS}}$ scheme can be used. Following Refs. [9, 10], we calculate the step scaling function in the RI-MOM scheme for the quark mass as below. Define a ratio

$$R_{\mathcal{O}}(\mu, a, m_q) = \frac{\Gamma_A(\mu, a, m_q)}{\Gamma_{\mathcal{O}}(\mu, a, m_q)} = \frac{Z_{\mathcal{O}}(\mu, a, m_q)}{Z_A}. \quad (25)$$

With Z_A determined, for example, as in Sec. 3.1, one can get the renormalization constant

$$Z_{\mathcal{O}}(\mu, a) = Z_A \lim_{m_q \rightarrow 0} R_{\mathcal{O}}(\mu, a, m_q). \quad (26)$$

A ratio of the $R_{\mathcal{O}}$'s at different scales is the step scaling function

$$\Sigma_{\mathcal{O}}(\mu, s\mu, a) = \lim_{m_q \rightarrow 0} \frac{R_{\mathcal{O}}(s\mu, a, m_q)}{R_{\mathcal{O}}(\mu, a, m_q)} = \lim_{m_q \rightarrow 0} \frac{Z_{\mathcal{O}}(s\mu, a, m_q)}{Z_{\mathcal{O}}(\mu, a, m_q)}. \quad (27)$$

Its continuum limit is

$$\sigma_{\mathcal{O}}(\mu, s\mu) = \lim_{a \rightarrow 0} \Sigma_{\mathcal{O}}(\mu, s\mu, a) = \frac{Z_{\mathcal{O}}(s\mu)}{Z_{\mathcal{O}}(\mu)}. \quad (28)$$

For the quark mass renormalization, using $Z_m = 1/Z_S$ we have

$$\Sigma_m(\mu, s\mu, a) = \lim_{m_q \rightarrow 0} \frac{Z_S(\mu, a, m_q)}{Z_S(s\mu, a, m_q)} = \frac{\lim_{m_q \rightarrow 0} Z_S(\mu, a, m_q)}{\lim_{m_q \rightarrow 0} Z_S(s\mu, a, m_q)}. \quad (29)$$

To calculate $\Sigma_m(\mu, s\mu, a)$ in the RI-MOM scheme, we use Z_S^{RI} which are already in the valance quark massless limit as computed in Sec. 3.3, for example, the black diamonds in the left panel of Fig. 6 for ensemble c005. After a linear extrapolation to the light sea quark massless limit ($m_l + m_{res} = 0$) of those Z_S^{RI} , we obtain $\Sigma_m(\mu, s\mu, a)$ by using interpolations explained below and Eq.(29).

The scales p in physical units for $Z_S^{\text{RI}}(a^2p^2, a)$ at our two lattice spacings do not exactly match in the data. Therefore we interpolate the lattice data $Z_S^{\text{RI}}(a^2p^2, a)$ in a^2p^2 with the ansatz

$$\frac{c_{-1}}{a^2p^2} + c_l \ln(a^2p^2) + c_0 + c_1(a^2p^2). \quad (30)$$

The first term in the above comes from the $1/p^2$ behavior of possible non-perturbative effects at low momenta. $c_1(a^2p^2)$ takes care of the discretization effects. The other terms mimic the running of the operator. We fit our data with the above ansatz in the whole range of momenta available. Then we interpolate to some physical scales $p = \mu$, which are chosen to be the same at the two lattice spacings.

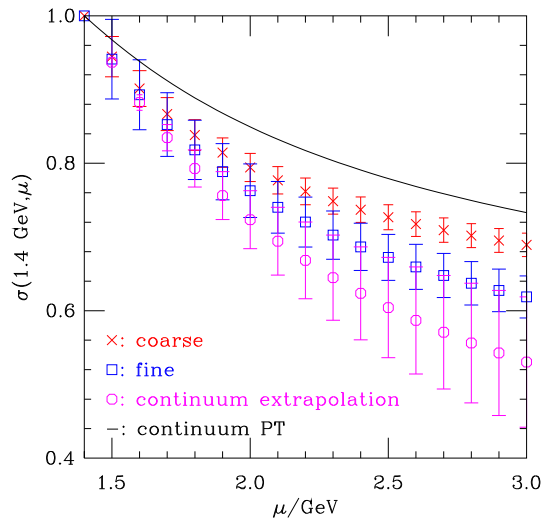


Figure 11: The step scaling function for Z_m and its value extrapolated to the continuum in the RI-MOM scheme.

Table 6: $Z_S^{\text{RI}}(\mu = 1.4 \text{ GeV})$ on the $24^3 \times 64$ and $32^3 \times 64$ lattices.

ensemble	c02	c01	c005	$m_l + m_{res} = 0$
$Z_S^{\text{RI}}(1.4 \text{ GeV})$	0.852(19)	0.782(14)	0.7317(72)	0.653(14)
ensemble	f008	f006	f004	$m_l + m_{res} = 0$
$Z_S^{\text{RI}}(1.4 \text{ GeV})$	0.772(18)	0.682(10)	0.6606(74)	0.606(11)

The step scaling function of the mass in the RI-MOM scheme from $\mu = 1.4 \text{ GeV}$ to a higher scale $s\mu$ which is in the range $[1.4 \text{ GeV}, 3 \text{ GeV}]$ is plotted in Fig. 11. We choose the relatively small value 1.4 GeV to follow Ref. [10]. Another reason is that $\mathcal{O}(a^2\mu^2)$ discretization errors are smaller at lower μ . In the graph the red crosses are the step scaling function on the coarse lattice, the blue squares are on the fine lattice. Then we consider the continuum limit of $\Sigma_m(\mu, s\mu, a)$ at given μ and $s\mu$. The magenta octagons are from linear extrapolations in a^2 to the continuum limit. Because there are only two lattice spacings, the extrapolated results have large error bars. The black curve is the 4-loop perturbative result for the RI-MOM scheme for comparison.

$Z_S^{\text{RI}}(\mu)$ at the physical scale $\mu = 1.4 \text{ GeV}$ (no a^2p^2 extrapolation as in Sec. 3.3 is performed) at the two lattice spacings can be obtained by interpolations. Fitting our RI scheme data (for example, black diamonds in the left panel of Fig. 6) with the ansatz Eq.(30) in the whole range of momenta available, we get $Z_S^{\text{RI}}(1.4 \text{ GeV}) = 0.7317(72)$ for ensemble c005. Similarly we obtain the values on other ensembles. Results on all ensembles are given in Tab. 6. A simultaneous fit to Z_S^{RI} using Eq.(23) to go to the light sea quark massless limit gives us the numbers in the last column of Tab. 6.

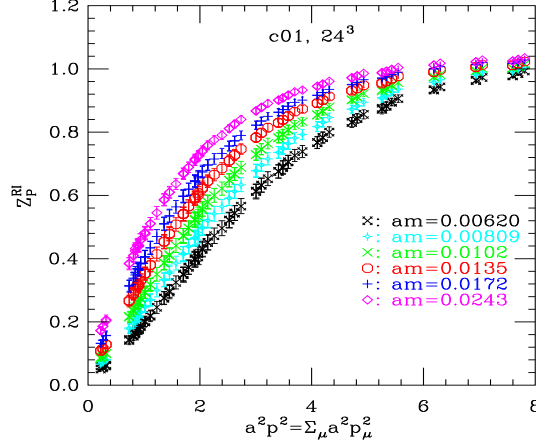


Figure 12: An example of Z_P^{RI} as a function of the momentum scale for ensemble c01 for different valence quark masses.

As we have calculated, the step scaling function in the continuum limit for the mass in the RI-MOM scheme is

$$\sigma_m(1.4 \text{ GeV}, 2 \text{ GeV}) = \frac{Z_m^{RI}(2 \text{ GeV})}{Z_m^{RI}(1.4 \text{ GeV})} = 0.723(39). \quad (31)$$

This can be used to run up to 2 GeV from 1.4 GeV after one gets the RI-MOM scheme quark masses in the continuum limit. The conversion ratio $Z_S^{\overline{\text{MS}}}/Z_S^{RI}$ from the RI to the $\overline{\text{MS}}$ scheme from Eq.(21) at 2 GeV is 1.289614, which can then be used to obtain quark masses in the $\overline{\text{MS}}$ scheme.

If we take the two numbers in the last column of Tab. 6, divide them by the number in Eq.(31) and convert to the $\overline{\text{MS}}$ scheme by using 1.289614, then we get 1.165(67) and 1.081(62) for the coarse and fine lattice respectively. They are in agreement with the two numbers in the last column of Tab. 4 although here the error bar is large.

3.5 Pseudoscalar density

The pseudoscalar renormalization constant Z_P^{RI} from Eq.(4) is shown in Fig. 12 for ensemble c01. Because of the coupling to the Goldstone boson channel [8], the projected vertex function Γ_P is divergent in the valence quark massless limit. This non-perturbative contamination is suppressed at large scale as $1/p^2$. The singular behavior in Z_P^{RI} at small $a^2 p^2$ as shown in Fig. 12 is due to this contamination. To remove this non-perturbative effect, we fit $1/Z_P^{RI}$ at each given $a^2 p^2$ to the ansatz [32]

$$Z_P^{-1} = \frac{A}{am_q} + B + C(am_q), \quad (32)$$

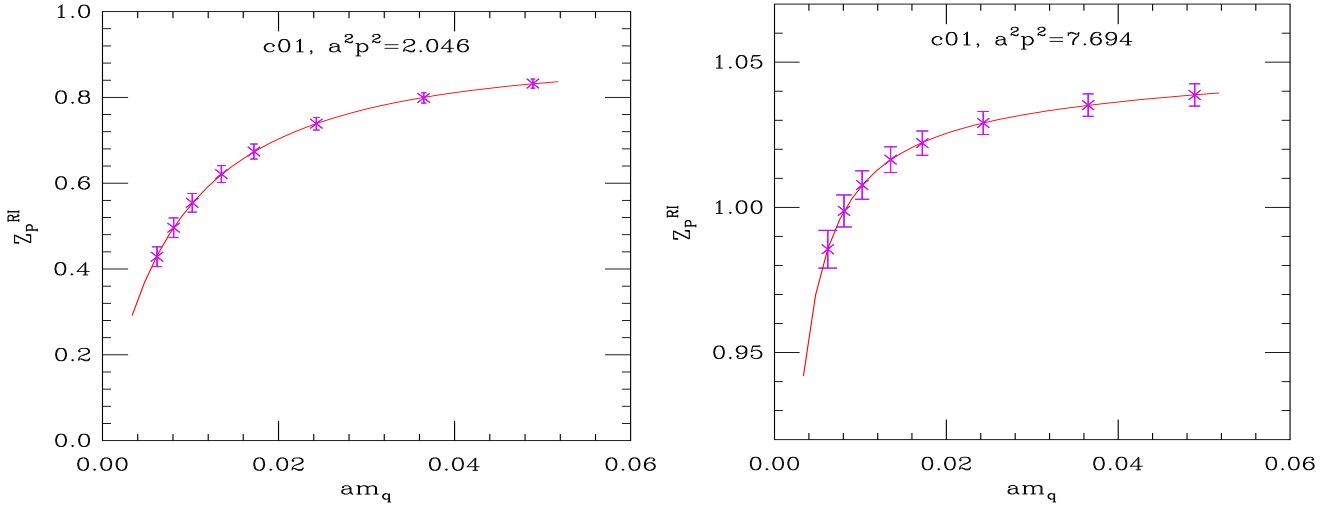


Figure 13: Examples of fittings of Z_P^{RI} to Eq.(32) for ensemble c01.

Table 7: $Z_{P,\overline{\text{MS}}}^{sub}(2 \text{ GeV})$ on the $24^3 \times 64$ and $32^3 \times 64$ lattices.

ensemble	c02	c01	c005	$m_l + m_{res} = 0$
$Z_{P,\overline{\text{MS}}}^{sub}(2 \text{ GeV})$	1.190(28)	1.164(22)	1.161(14)	1.138(25)
ensemble	f008	f006	f004	$m_l + m_{res} = 0$
$Z_{P,\overline{\text{MS}}}^{sub}(2 \text{ GeV})$	1.102(24)	1.089(19)	1.065(21)	1.063(21)

where A, B and C are three fit parameters. Then $Z_P^{sub} = B^{-1}$ is the value we take in the valence quark chiral limit.

In Fig. 13 we show some examples of the fitting of Z_P^{RI} to Eq.(32) at some given $a^2 p^2$. All the fittings have small χ^2/dof . After obtaining Z_P^{sub} in the RI scheme, we use Eq.(21) to convert to the $\overline{\text{MS}}$ scheme. The results are shown by the red fancy crosses in Fig. 14. Similar to the analysis of Z_S , we use the quark mass anomalous dimension to evolve $Z_{P,\overline{\text{MS}}}^{sub}(a^2 p^2)$ to 2 GeV in the $\overline{\text{MS}}$ scheme and obtain the blue crosses in Fig. 14. Then a linear fit in $a^2 p^2$ (the blue solid line in Fig. 14) to the data at $a^2 p^2 > 5$ is used to extrapolate away $\mathcal{O}(a^2 p^2)$ discretization errors. We finally find $Z_{P,\overline{\text{MS}}}^{sub} = 1.164(22)$ at 2 GeV on ensemble c01.

The values of $Z_{P,\overline{\text{MS}}}^{sub}(2 \text{ GeV})$ on all ensembles are collected in Tab. 7. In the last column of Tab. 7, the sea quark massless limit values of $Z_{P,\overline{\text{MS}}}^{sub}$ are given. They are obtained from a simultaneous linear extrapolation in the renormalized light sea quark mass to $Z_{P,\overline{\text{MS}}}^{sub}$ on both $L = 24$ and 32 lattices. The extrapolation is shown in Fig. 15 with the fit function given in Eq.(23). Comparing the numbers in Tab. 7 with those in Tab. 4, we see that $Z_S = Z_P^{sub}$ is well

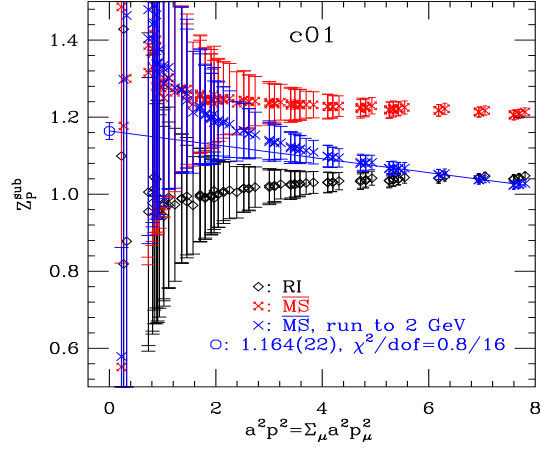


Figure 14: The conversion and running of Z_P^{sub} in the valence quark massless limit on ensemble c01. The black diamonds are the values in the RI scheme. The red fancy crosses are those in the \overline{MS} scheme. The blue crosses are the results evolved to 2 GeV in the \overline{MS} scheme as a function of the initial renormalization scale.

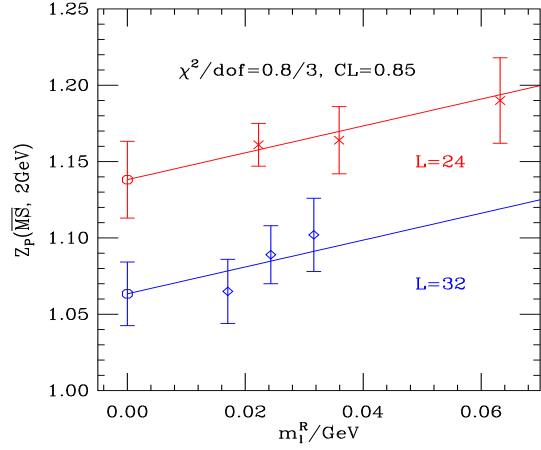


Figure 15: Linear extrapolation of $Z_{P,\overline{MS}}^{sub}$ to the light sea quark massless limit.

Table 8: Error budget of $Z_{P,\overline{\text{MS}}}^{sub}(2 \text{ GeV})$ in the chiral limit

Source	Error (%,L=24)	Error (%,L=32)
Statistical	2.2	2.0
Truncation (RI to $\overline{\text{MS}}$)	1.5	1.4
Coupling constant	0.3	0.3
Perturbative running	<0.02	<0.02
Lattice spacing	0.5	0.4
Fit range of a^2p^2	0.1	0.1
Extrapolation in m_l^R	0.6	3.8
Total systematic uncertainty	1.7	4.1

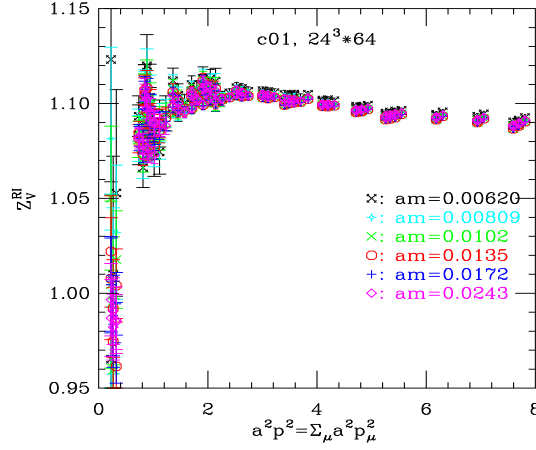


Figure 16: Examples of Z_V^{RI} as functions of the momentum scale for ensemble c01.

satisfied within errors.

Similar to the analysis for Z_S , we summarize the systematic errors as well as the statistical error in Tab. 8. Unlike $Z_S^{\overline{\text{MS}}}$, the statistical error of $Z_{P,\overline{\text{MS}}}^{sub}$ is about the same size as the systematic error.

3.6 Vector current

The renormalization constant in the RI scheme for the local vector current for different valence quark masses on data ensemble c01 are shown in Fig. 16. Here in using Eq.(4), we have averaged $\mu = 1, 2, 3, 4$ for the vector current. The valence quark mass dependence for Z_V^{RI} is small so that the symbols in Fig. 16 for different masses are almost on top of each other. Z_V^{RI} is scale independent when the renormalization scale is big. This is confirmed in Fig. 16. At scales $a^2 p^2 > \sim 3$, Z_V^{RI} is

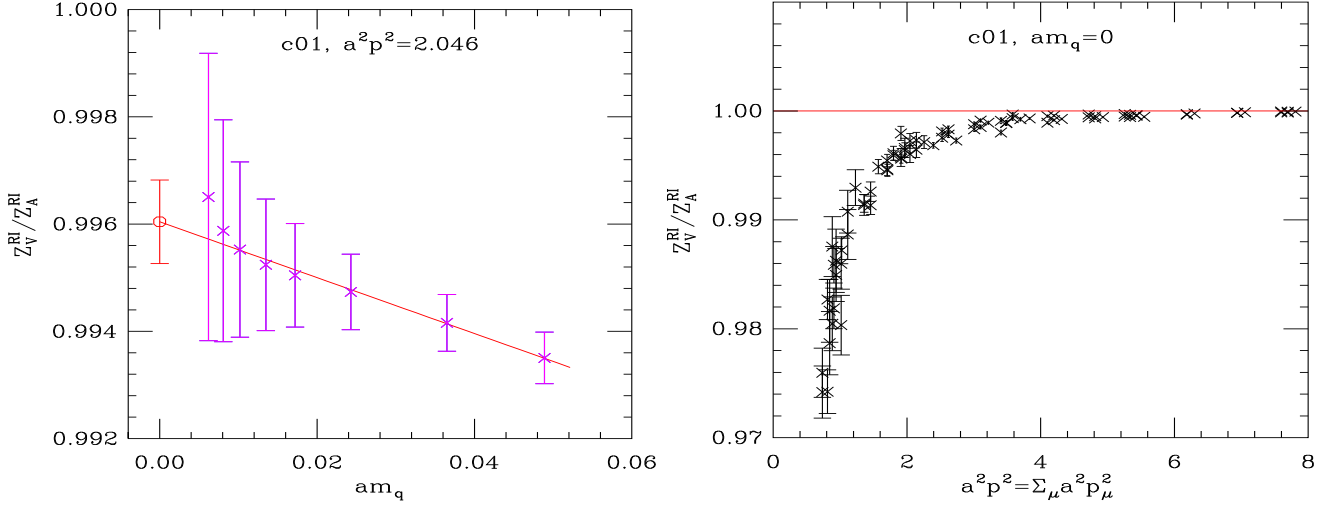


Figure 17: Left panel: Z_V^{RI}/Z_A^{RI} against the valence quark mass from ensemble c01 at a certain momentum scale and a linear extrapolation to $am_q = 0$. Right panel: Z_V^{RI}/Z_A^{RI} in the valence quark massless limit as a function of the momentum scale for ensembles c01.

flat up to discretization errors.

In Fig. 17, the ratio Z_V^{RI}/Z_A^{RI} for ensemble c01 is shown. To go to the chiral limit, we use a linear extrapolation in valence quark mass for Z_V^{RI}/Z_A^{RI} . The left panel in Fig. 17 shows an example of such extrapolations. As we can see on the right panel of Fig. 17, at large momentum scales, $Z_V^{RI}/Z_A^{RI} = 1$, i.e., $Z_V^{RI} = Z_A^{RI}$ is satisfied as expected.

The results of Z_V^{RI}/Z_A^{RI} for other five ensembles are similar to those for ensemble c01.

4 Summary

In this work, we obtain the renormalization constants for quark bilinear operators for the setup of overlap valence quark on 2+1-flavor domain wall fermion configurations. We calculate those constants non-perturbatively by using Ward identity and the RI-MOM scheme. The matching factors from the lattice to the continuum $\overline{\text{MS}}$ scheme for the scalar, pseudoscalar, vector and axial vector currents are obtained. $Z_S = Z_P$ and $Z_V = Z_A$ are confirmed for overlap fermions. The step scaling function of quark masses in the RI-MOM scheme is also calculated. By using the step scaling function in the continuum limit, the renormalized quark mass in the RI-MOM scheme can be run up to a high scale and then be converted to the $\overline{\text{MS}}$ scheme. Our main results are collected in Tabs. 3, 4, 5, 6, 7 and 8. These matching factors are important components in lattice determination of physical quantities such as quark masses, quark condensate and pseudoscalar meson decay constants.

The statistical error of Z_S can reach less than one percent, which is much smaller than its

systematic error. A big contribution of the systematic error comes from the perturbative conversion ratio from the RI-MOM scheme to the $\overline{\text{MS}}$ scheme. The RI-SMOM scheme [33] was shown to have conversion ratios which converge much faster [34, 35] and smaller non-perturbative effects. In the RI-SMOM scheme, the momentum magnitudes of the Green functions of the relevant operators are symmetric. However in this work our boundary condition in the time direction is anti-periodic. This limits the number of symmetric momentum combinations (actually we cannot have exact symmetric momentum combinations). To shrink the systematic error, one can use a periodic boundary condition in the time direction or twisted boundary conditions [9] with the RI-SMOM scheme.

Acknowledgements

We thank RBC-UKQCD collaboration for sharing the domain wall fermion configurations. ZL thanks Thomas DeGrand, Ron Horgan and Olivier Pène for useful discussions. This work is partially supported by U.S. DOE Grant No. DE-FG05-84ER40154 and by the National Science Foundation of China (NSFC) under Grants 11105153, 10835002, 11075167, 11275169 and 11335001. ZL is partially supported by the Youth Innovation Promotion Association of CAS. YC and ZL acknowledge the support of NSFC and DFG (CRC110).

References

- [1] M. Gong, A. Alexandru, Y. Chen, T. Doi, S. J. Dong, T. Draper, W. Freeman and M. Glatzmaier *et al.*, Phys. Rev. D **88**, **014503** (2013) [[arXiv:1304.1194](#) [hep-ph]].
- [2] S.J. Dong, F.X. Lee, K.F. Liu, and J.B. Zhang, Phys. Rev. Lett. **85**, 5051 (2000).
- [3] T. Draper, N. Mathur, J. Zhang, A. Alexandru, Y. Chen, S. -J. Dong, I. Horvath, F. Lee and S. Tamhankar, PoS LAT **2005**, 120 (2006) [[hep-lat/0510075](#)].
- [4] K. F. Liu and S.-J. Dong, Int.J.Mod.Phys. A **20**, 7241 (2005).
- [5] A. Li, A. Alexandru, Y. Chen, T. Doi, S.J. Dong, T. Draper, M. Gong, A. Hasenfratz, I. Horvath, F. X. Lee, K. F. Liu, N. Mathur, T. Streuer and J. B. Zhang, Phys. Rev. D **82**, 114501 (2010) [[arXiv:1005.5424](#) [hep-lat]].
- [6] A. Hasenfratz and F. Knechtli, Phys. Rev. D **64**, 034504 (2001) [[hep-lat/0103029](#)].
- [7] Y. B. Yang, Y. Chen, A. Alexandru, S. J. Dong, T. Draper, M. Gong, F. X. Lee and A. Li *et al.*, [arXiv:1401.1487](#) [hep-lat].
- [8] G. Martinelli, C. Pittori, C. T. Sachrajda, M. Testa and A. Vladikas, Nucl. Phys. B **445** (1995) 81 [[arXiv:hep-lat/9411010](#)].

- [9] R. Arthur *et al.* [RBC and UKQCD Collaborations], Phys. Rev. D **83**, 114511 (2011) [arXiv:1006.0422 [hep-lat]].
- [10] R. Arthur, P. A. Boyle, S. Hashimoto and R. Hudspith, Phys. Rev. D **88**, 114506 (2013) [arXiv:1306.0835 [hep-lat]].
- [11] J. B. Zhang, N. Mathur, S. J. Dong, T. Draper, I. Horvath, F. X. Lee, D. B. Leinweber, K. F. Liu and A. G. Williams, Phys. Rev. D **72**, 114509 (2005) [hep-lat/0507022].
- [12] H. Neuberger, Phys. Lett. B **417**, 141 (1998) [hep-lat/9707022].
- [13] T. -W. Chiu and S. V. Zenkin, Phys. Rev. D **59**, 074501 (1999) [hep-lat/9806019].
- [14] Y. Aoki *et al.* [RBC and UKQCD Collaborations], Phys. Rev. D **83**, 074508 (2011) [arXiv:1011.0892 [hep-lat]].
- [15] C. Allton *et al.* [RBC-UKQCD Collaboration], Phys. Rev. D **78**, 114509 (2008) [arXiv:0804.0473 [hep-lat]].
- [16] F. de Soto and C. Roiesnel, JHEP **0709**, 007 (2007) [arXiv:0705.3523 [hep-lat]].
- [17] B. Blossier, P. Boucaud, M. Brinet, F. De Soto, Z. Liu, V. Morenas, O. Pene and K. Petrov *et al.*, Phys. Rev. D **83**, 074506 (2011) [arXiv:1011.2414 [hep-ph]].
- [18] M. Constantinou, M. Costa, M. Göckeler, R. Horsley, H. Panagopoulos, H. Perlt, P. E. L. Rakow and G. Schierholz *et al.*, Phys. Rev. D **87**, 096019 (2013) [arXiv:1303.6776 [hep-lat]].
- [19] M. Göckeler, R. Horsley, H. Oelrich, H. Perlt, D. Petters, P. E. L. Rakow, A. Schafer and G. Schierholz *et al.*, Nucl. Phys. B **544**, 699 (1999) [hep-lat/9807044].
- [20] T. Blum, N. H. Christ, C. Cristian, C. Dawson, G. T. Fleming, G. Liu, R. Mawhinney and A. Soni *et al.*, Phys. Rev. D **66**, 014504 (2002) [hep-lat/0102005].
- [21] Y. Aoki, P. A. Boyle, N. H. Christ, C. Dawson, M. A. Donnellan, T. Izubuchi, A. Juttner and S. Li *et al.*, Phys. Rev. D **78**, 054510 (2008) [arXiv:0712.1061 [hep-lat]].
- [22] T. A. DeGrand and Z. Liu, Phys. Rev. D **72**, 054508 (2005) [hep-lat/0507017].
- [23] E. Franco and V. Lubicz, Nucl. Phys. B **531** (1998) 641 [arXiv:hep-ph/9803491].
- [24] K. G. Chetyrkin and A. Retey, Nucl. Phys. B **583** (2000) 3 [arXiv:hep-ph/9910332].
- [25] A. I. Alekseev, Few Body Syst. **32**, 193 (2003) [hep-ph/0211339].
- [26] T. van Ritbergen, J. A. M. Vermaseren and S. A. Larin, Phys. Lett. B **400**, 379 (1997) [hep-ph/9701390].

- [27] J. Beringer *et al.* [Particle Data Group Collaboration], Phys. Rev. D **86**, 010001 (2012).
- [28] Y. Aoki, PoS LAT **2009**, 012 (2009) [[arXiv:1005.2339](#) [hep-lat]].
- [29] C. Aubin, J. Laiho and R. S. Van de Water, Phys. Rev. D **81**, 014507 (2010) [[arXiv:0905.3947](#) [hep-lat]].
- [30] R. Gupta, T. Bhattacharya, A. Joseph, S. D. Cohen and H. -W. Lin, PoS LATTICE **2013**, 409 (2014) [[arXiv:1403.2447](#) [hep-lat]].
- [31] Y. Aoki, R. Arthur, T. Blum, P. A. Boyle, D. Brommel, N. H. Christ, C. Dawson and T. Izubuchi *et al.*, Phys. Rev. D **84**, 014503 (2011) [[arXiv:1012.4178](#) [hep-lat]].
- [32] D. Becirevic, V. Gimenez, V. Lubicz, G. Martinelli, M. Papinutto and J. Reyes, JHEP **0408**, 022 (2004) [[hep-lat/0401033](#)].
- [33] C. Sturm, Y. Aoki, N. H. Christ, T. Izubuchi, C. T. C. Sachrajda and A. Soni, Phys. Rev. D **80**, 014501 (2009) [[arXiv:0901.2599](#) [hep-ph]].
- [34] M. Gorbahn and S. Jager, Phys. Rev. D **82**, 114001 (2010) [[arXiv:1004.3997](#) [hep-ph]].
- [35] L. G. Almeida and C. Sturm, Phys. Rev. D **82**, 054017 (2010) [[arXiv:1004.4613](#) [hep-ph]].